

# Lithium-ion battery recycling through an integrated electro-membrane crystallization technology

Received: 25 April 2025

Accepted: 5 December 2025

Cite this article as: Zhao, Y., Qiu, Y., Xia, L. *et al.* Lithium-ion battery recycling through an integrated electro-membrane crystallization technology. *Nat Commun* (2025). <https://doi.org/10.1038/s41467-025-67678-5>

Yan Zhao, Yangbo Qiu, Lei Xia, Xi Zhang, Shuang Zheng, Gang Lu, Jin Shang, Raf Dewil, Seth B. Darling, Bart Van der Bruggen & Chuyang Tang

We are providing an unedited version of this manuscript to give early access to its findings. Before final publication, the manuscript will undergo further editing. Please note there may be errors present which affect the content, and all legal disclaimers apply.

If this paper is publishing under a Transparent Peer Review model then Peer Review reports will publish with the final article.

## Lithium-ion battery recycling through an integrated electro-membrane crystallization technology

Yan Zhao <sup>1,2,||,\*</sup>, Yangbo Qiu <sup>1,||</sup>, Lei Xia <sup>3,||</sup>, Xi Zhang <sup>4,5</sup>, Shuang Zheng <sup>1</sup>, Gang Lu <sup>6</sup>, Jin Shang <sup>7</sup>, Raf Dewil <sup>8,9</sup>, Seth B. Darling <sup>4,5</sup>, Bart Van der Bruggen <sup>2,10,11,\*</sup>, Chuyang Tang<sup>1,\*</sup>

<sup>1</sup>Department of Civil Engineering, The University of Hong Kong, Pokfulam, SAR 999077, Hong Kong.

<sup>2</sup>Department of Chemical Engineering, KU Leuven, Celestijnenlaan 200F, B-3001 Leuven, Belgium.

<sup>3</sup>Division of Soil and Water Management, KU Leuven, Kasteelpark Arenberg 20, B-3001 Leuven, Belgium.

<sup>4</sup>Pritzker School of Molecular Engineering, University of Chicago, Chicago, Illinois 60637, United States.

<sup>5</sup>Chemical Sciences and Engineering Division, Argonne National Laboratory, Lemont, Illinois 60439, United States.

<sup>6</sup>Department of Chemical and Biomolecular Engineering, University of Pennsylvania, Philadelphia, PA 19104, United States.

<sup>7</sup>School of Energy and Environment, City University of Hong Kong, Tat Chee Avenue, Kowloon, Hong Kong.

<sup>8</sup>Department of Chemical Engineering, KU Leuven, Process and Environmental Technology Lab, J. De Nayerlaan 5, 2860 Sint-Katelijne-Waver, Belgium.

<sup>9</sup>Department of Engineering Science, University of Oxford, Parks Road, Oxford OX1 3PJ, United Kingdom.

<sup>10</sup>Department of Chemical and Biochemical Engineering, Korea University, 145 Anam-Ro, Sungbuk-Gu, Seoul 02841, Republic of Korea.

<sup>11</sup>Nanotechnology Centre, CEET, VSB-Technical University of Ostrava, 17. listopadu 2172/15, 708 00 Ostrava – Poruba, Czechia.

**||Contributed equally:** Y. Zhao, Y. Qiu and L. Xia contributed equally to this study.

**\*Corresponding authors:**

yanzhaox@hku.hk (Y. Zhao)

bart.vanderbruggen@kuleuven.be (B. Van der Bruggen)

tangc@hku.hk (C. Tang)

### Abstract

Lithium-ion battery (LIB) recycling is crucial for energy security, environmental sustainability, and economic viability, as the finite lifespan of LIBs results in a significant annual accumulation of spent units. However, effectively and precisely recovering valuable metal ions such as  $\text{Li}^+$ ,  $\text{Mn}^{2+}$ ,  $\text{Ni}^{2+}$  and  $\text{Co}^{2+}$  from complex LIB leaching solutions remains a major challenge. Here, we present a scalable electro-membrane crystallization-assisted general recycling (e-MCGR) technology for the selective and efficient recovery of those metal ions from LIB leaching solutions. By synergistically integrating electrochemical and electro-membrane technologies, our proposed technology incorporates four key configurations: selective membrane dual-stage distillation, bipolar membrane in-situ crystallization, membrane metal-complexing ex-situ crystallization, and membrane metal-extracting temporal crystallization. We systematically analyze the metal-ion transfer kinetics of electro-membranes (ion selectivity and permeation rates) and the performance of electro-membrane crystallization systems (recovery rates and product purity), alongside evaluating energy consumption, economic viability, and environmental benefits. Our optimized e-MCGR process achieves a recovery of 95.5% for  $\text{Li}^+$ , 99.5% for  $\text{Mn}^{2+}$ , 83.1% for  $\text{Ni}^{2+}$ , and 87.3% for  $\text{Co}^{2+}$ , yielding high product purities of 99.9% for  $\text{Li}_2\text{CO}_3$ , 99.9% for  $\text{Mn}_3\text{O}_4$ , 99.5% for  $\text{Ni}(\text{OH})_2$  and 92.5% for  $\text{Co}(\text{OH})_2$ . The e-MCGR technology demonstrates significant potential to reshape LIB recycling paradigms, aligning technological efficiency with energy, environmental and economic sustainability.

## Introduction

Lithium-ion batteries (LIBs), the powerhouse of modern electronics, have been a global cornerstone to power billions of electronic devices<sup>1</sup>. They have undergone exponential and fast development in adding resilience to electrical grids with increasing contributions from intermittent sources<sup>2,3</sup>. By 2024, global LIB production reached approximately 3,950.0 gigawatt-hours (GWh), with China contributing over 2,677 GWh of this output, which represented over 65% of the global market share (Fig. 1a). Such rapid expansion of the LIB production underscores China's success in reducing reliance on carbon-based energy while advancing renewable energy adoption (Supplementary Fig. 1). Unfortunately, the finite lifespan of these batteries (typically 2-9 years, around 500-3000 cycles) results in a substantial annual accumulation of spent batteries<sup>4</sup>. According to the data, the global generation of spent LIBs surged 1700 Kilotons (Kt) in 2024, with the volumes expected to rise further as demand grows (Supplementary Fig. 3). This escalating influx of spent batteries poses critical energy, economic, and environmental challenges, particularly in major economies with high LIB usage, such as China, the United States, European nations, Japan, and Korea (Fig. 1b and Supplementary Fig. 2).

The efficient recycling of spent batteries has become an imperative priority<sup>5-7</sup>. Among the complex composition of spent LIBs, the recovery of high-value metal ions, such as  $\text{Li}^+$ ,  $\text{Mn}^{2+}$ ,  $\text{Ni}^{2+}$  and  $\text{Co}^{2+}$ , offers a potential opportunity for resource reclamation<sup>8,9</sup>. Typically, spent LIBs are dissolved in acidic solutions, followed by pH adjustment to obtain a leaching solution<sup>10</sup>, from which metal ions need to be recovered efficiently and precisely. To address these challenges, various approaches such as adsorption, ion exchange, solvent extraction, precipitation, or evaporative crystallization have been explored<sup>11-14</sup>. While some of these methods enable metal ion recovery, their limitations stem from imprecise separation and inefficient purification<sup>15,16</sup>. Thus, achieving metal ion recovery with both high recovery and high-purity products in a sustainable manner remains a significant

hurdle. Additionally, most existing approaches focus narrowly on technical aspects, often overlooking system-level integration and sustainability<sup>17-19</sup>.

In recent decades, membrane technologies with tunable structures and functional groups have shown great promise as an efficient method for ion separation<sup>20-22</sup>. Among them, electrodialysis, by using electro-membranes, has emerged as a viable approach for recovering ion resources from diverse streams<sup>23-25</sup>. Advances in material science have led to the development of electro-membranes with tailored ion selectivity, enabling precise targeting of specific ions even in the presence of competing species with similar physicochemical properties<sup>26-30</sup>. However, ion transport across the electro-membranes is constrained by their ion-transfer kinetics (e-MK), resulting in trade-offs between ion selectivity and permeation rates<sup>13,31-33</sup>. Notably, recent research efforts have been directed towards combining electrochemical systems with crystallization to enhance metal ion recovery, resulting in the development of electrochemical crystallization. This approach enables simultaneous metal ion separation and crystal product generation<sup>24,34-36</sup>. Yet, a trade-off between the high ion recovery rate and product purity exists at the process scale<sup>37,38</sup>. To address this, hybridizing electrochemical systems with electro-membrane technology and crystallization technology (e-MC) offers a promising pathway for achieving metal ions with both high recoveries and high product purities. Previously, membrane technologies have relied on principles such as size exclusion, electrostatic interactions, and chemical affinity to achieve ion selectivity<sup>31,40-42</sup>. Although substantial progress has been made toward developing membranes with precise single-ion selectivity, their utility in real-world resource recovery remains limited by material constraints and has largely been tested only in isolated/single systems<sup>43-45</sup>. Furthermore, their applicability in LIB recycling has not been convincingly demonstrated<sup>42,46</sup>.

To bridge this gap, we propose an e-MC-assisted general recycling (e-MCGR) concept, which integrates mature membranes into a closed-loop and modular framework tailored for spent LIB

recycling. The e-MCGR concept is designed to address both separation precision and practical applicability while maintaining high recovery and product purity. As illustrated in Fig. 2, the process begins with disassembly and acidic dissolution of spent LIBs, followed by pH adjustment ( $\sim 7$ ) to generate a representative leaching solution<sup>47</sup>. Valuable metals ions, such as  $\text{Li}^+$ ,  $\text{Mn}^{2+}$ ,  $\text{Ni}^{2+}$  and  $\text{Co}^{2+}$ , are then selectively recovered through a three-part process: (i) separation of monovalent cations ( $\text{Li}^+$  and  $\text{Na}^+$ ) from divalent cations ( $\text{Mn}^{2+}$ ,  $\text{Ni}^{2+}$  and  $\text{Co}^{2+}$ ) through selective membrane dual-stage distillation; (ii), separation of monovalent cations from each other (separation  $\text{Li}^+$  and  $\text{Na}^+$ ) and  $\text{Li}^+$  crystallization via bipolar membrane in-situ crystallization and (iii) selective recovery of  $\text{Mn}^{2+}$ ,  $\text{Ni}^{2+}$  and  $\text{Co}^{2+}$  by membrane metal-complexing ex-situ crystallization and membrane metal-extracting temporal crystallization. These processes enable the recovery of high-purity  $\text{Li}_2\text{CO}_3$ ,  $\text{Mn}_3\text{O}_4$ ,  $\text{Ni}(\text{OH})_2$ , and  $\text{Co}(\text{OH})_2$ . Despite the strategic importance of metal ion recovery from spent LIBs, no comprehensive study or design has yet explored a fully sustainable LIB recycling through this e-MCGR concept. Furthermore, the potential of LIB recycling to enhance energy security, environmental sustainability, and economic viability remains insufficiently explored. This e-MCGR presents an innovative framework and practical strategy for optimizing metal ion recovery, thereby addressing the challenges encountered in sustainable resource recovery from LIBs. Given the global scale of LIB development, this e-MCGR concept and approach contribute a holistic, scalable, and sustainable solution to address global challenges in LIB waste management and resource recovery.

## Results

### Separation of monovalent cations from divalent cations

The e-MCGR starts with ultrafiltration (UF, Supplementary Table 5), where the organic pollutants in the feed are removed to minimize membrane clogging. Then the metal ions in the feed are concentrated using reverse osmosis (RO, Supplementary Table 6) before entering the ED cell due to low metal ion concentration in spent LIB leaching solutions (Fig. 2, Supplementary Table

7). Due to the unique thermodynamic and physical characteristics of metal ions, such as specific hydrated diameters and hydration energy (Supplementary Table 8), monovalent metal ions ( $\text{Li}^+$  and  $\text{Na}^+$ ) can be separated from multivalent metal ions ( $\text{Mn}^{2+}$ ,  $\text{Ni}^{2+}$  and  $\text{Co}^{2+}$ ). Recent advancements have enabled the use of commercial monovalent ion-selective electro-membranes, which operate based on mechanisms such as size exclusion and electrostatic repulsion (Fig. 3a and Supplementary Fig. 5). To efficiently recover those valuable metal ions,  $\text{Li}^+$  and  $\text{Na}^+$  are separated from  $\text{Mn}^{2+}$ ,  $\text{Ni}^{2+}$  and  $\text{Co}^{2+}$  through continuous selective electro-dialysis. The separation is firstly evidenced by the change in color of the leaching solution (Fig. 3b), where the dark brown of the leaching solution is changed to a dark red solution containing  $\text{Mn}^{2+}$ ,  $\text{Ni}^{2+}$  and  $\text{Co}^{2+}$ , while the solution containing only  $\text{Li}^+$  and  $\text{Na}^+$  is colorless.

To enhance separation efficiency, a multi-stage selective electro-dialysis could be employed<sup>48</sup>, but it is limited by practical constraints in metal ion recovery rates and the trade-offs in energy, economic, and environmental benefits<sup>49</sup>. Therefore, a more suitable two-stage selective electro-dialysis configuration is designed here, termed as selective membrane dual-stage distillation (Supplementary Fig. 6). The impact of current density on e-MK is evaluated by using three current densities (i.e., 1.0, 2.5 and 5.0  $\text{mA cm}^{-2}$ ). In the first-stage selective electro-dialysis at operating condition of 1.0  $\text{mA cm}^{-2}$  with 4 L of leaching solutions in the feed chamber, the concentrations of  $\text{Li}^+$  and  $\text{Na}^+$  increase in the recovery chamber (Fig. 3c). In this configuration, multivalent metal ions ( $\text{Mn}^{2+}$ ,  $\text{Ni}^{2+}$  and  $\text{Co}^{2+}$ ) are rejected by the selective membranes, while  $\text{Li}^+$  and  $\text{Na}^+$  readily permeate (Supplementary Fig. 7). However, residual  $\text{Mn}^{2+}$  (0.06  $\text{g L}^{-1}$ ),  $\text{Ni}^{2+}$  (0.06  $\text{g L}^{-1}$ ) and  $\text{Co}^{2+}$  (0.07  $\text{g L}^{-1}$ ) mixed with amounts of  $\text{Na}^+$  (0.04  $\text{g L}^{-1}$ ) and  $\text{Li}^+$  (0.14  $\text{g L}^{-1}$ ) in transitional chambers necessitate further separation due to the limited selectivity of commercial membranes. Thus, the 2 L transitional solutions (in transitional chamber-1 and transitional chamber-2) from the first-stage selective electro-dialysis are fed into the second-stage selective electro-dialysis for additional separation (Fig. 3d). This selective membrane dual-stage distillation configuration proves optimal for separating  $\text{Li}^+$  and  $\text{Na}^+$  from  $\text{Mn}^{2+}$ ,  $\text{Ni}^{2+}$  and  $\text{Co}^{2+}$ . With the combination of first-

stage operating at  $1 \text{ mA cm}^{-2}$  and second-stage at  $0.5 \text{ mA cm}^{-2}$ , this dual-stage distillation achieves the highest accumulative recoveries of 96.5% for  $\text{Li}^+$  and 96.4% for  $\text{Na}^+$ , while completely rejecting  $\text{Mn}^{2+}$ ,  $\text{Ni}^{2+}$  and  $\text{Co}^{2+}$  (Fig. 3e and Supplementary Fig. 8).

Effectively, the transport of metal ions from the feed chamber to the recovery chamber is governed by e-MK and reflected by voltage change (Supplementary Fig. 9). Regardless of stages or operating conditions, the e-MK is the critical factor for determining metal ion selectivity, permeation rate, and ultimately, recovery and purity. Although additional stages could enhance metal ion recovery purity, they lead to higher losses of  $\text{Li}^+$  and  $\text{Na}^+$  in the transitional chamber and higher energy consumption. Thus, the selective membrane dual-stage distillation technology strikes an optimal balance for separating monovalent cations ( $\text{Li}^+$  and  $\text{Na}^+$ ) and multivalent cations ( $\text{Mn}^{2+}$ ,  $\text{Ni}^{2+}$  and  $\text{Co}^{2+}$ ) with current membrane technologies.

A comprehensive evaluation of energy consumption, economic profitability, and environmental benefits is conducted for this selective membrane dual-stage distillation configuration (Supplementary Fig. 10). With this optimized configuration, most of this energy is consumed by metal ion transport in membranes. For this selective membrane dual-stage distillation, key metrics, such as energy consumption (EC), energy cost ( $C_e$ ), investment cost ( $C_i$ ),  $\text{Li}^+$  recovery cost ( $C_{\text{Li}}$ ), monovalent metal ion recovery rate ( $R_m$ ) and purity of recovered  $\text{Li}^+$  ( $P_{\text{Li}}$ ) are analysed and summarized (Supplementary Fig. 10 and Supplementary Table 9). For the first-stage selective electrodialysis, the impact of current density on separation kinetics is evaluated at 1.0, 2.5 and  $5.0 \text{ mA cm}^{-2}$ . At  $1.0 \text{ mA cm}^{-2}$ , the system demonstrated the lowest energy cost ( $1.24 \text{ \$ kg}^{-1}$ ), investment cost ( $3.78 \text{ \$ kg}^{-1}$ ), and the energy consumption ( $11.83 \text{ kWh kg}^{-1}$ ), along with the highest monovalent cation recovery rate (87.7%), compared to 66.8% and 60.5% at 2.5 and  $5.0 \text{ mA cm}^{-2}$ , respectively (Fig. 3f). To further enhance  $\text{Li}^+$  recovery, transitional solutions from the first-stage selective electrodialysis are processed in a second-stage selective electrodialysis operated at a lower current density ( $0.5 \text{ mA cm}^{-2}$ ). Based on the operating conditions and the expenditure per 1 kg of  $\text{LiCl}$  recovery, this configuration achieves around 96.5% recovery of

monovalent metal ions ( $\text{Li}^+$  and  $\text{Na}^+$ ), with an energy cost of  $2.73 \text{ \$ kg}^{-1}$ , investment cost of  $13.25 \text{ \$ kg}^{-1}$ , and energy consumption of  $15.97 \text{ kWh kg}^{-1}$  (Fig. 3g). This initial separation of monovalent and multivalent cations is essential for efficient resource recovery, both technologically and in terms of energy, economic, and environmental reasons. While selective membrane dual-stage distillation technology achieves a high separation efficiency, current commercial membranes are limited by their metal ion throughput. In addition, they suffer from severe membrane scaling (Supplementary Fig. 11 and Fig. 12). On the one hand, this scaling can be attributed to the inherent poor anti-scaling properties of commercial electro-membrane. On the other hand, water splitting may occur on the CIMS surface as most divalent ions are electrostatically repelled and cannot serve as current carriers. The resulting shortage of charge carriers induces forced dissociation of water into  $\text{H}^+$  and  $\text{OH}^-$ , with  $\text{OH}^-$  reacting with accumulated metal ions to form insoluble hydroxide precursors that deposit on the membrane surface (Supplementary Fig. 13).

### **Recovery of $\text{Li}^+$ and $\text{Na}^+$**

Following the initial separation configuration, the recovered feed contains only monovalent metal ions ( $\text{Li}^+$  and  $\text{Na}^+$ ), yet the lack of highly  $\text{Li}^+$ -selective electro-membranes poses a significant challenge, and current electrodialysis cannot achieve crystallization. Our innovative approach offers a solution that enables simultaneous metal ion separation and crystallization of  $\text{Li}_2\text{CO}_3$ . Typically,  $\text{CO}_2$  is captured by reacting with  $\text{OH}^-$ , a method commonly employed for carbon capture and storage, and utilized as a carbonate source. Leveraging the bipolar membrane electrodialysis, an in-situ crystallization configuration is developed to separate  $\text{Li}^+$  from  $\text{Na}^+$  while generating high-purity  $\text{Li}_2\text{CO}_3$  crystals (Supplementary Fig. 14). In this system,  $\text{CO}_2$  is captured via a membrane contactor (Supplementary Fig. 15) and reacts with the  $\text{OH}^-$  generated in-situ by the bipolar membrane (chemical reaction pathways are detailed in Supplementary Fig. 16). This hybridization of bipolar membrane and in-situ crystallization technologies ensures  $\text{Li}^+$  capture,  $\text{CO}_2$  utilization, and  $\text{Li}_2\text{CO}_3$  production (Fig. 4a and Supplementary Fig. 17).

Fig. 4b illustrates the mechanisms of the bipolar membrane in-situ crystallization process, culminating in the formation of white powder products. Scanning electron microscopy (SEM) reveals that the precipitated powders exhibit a regular octahedral crystal structure with an average diameter of 4  $\mu\text{m}$  (Fig. 4c and Supplementary Fig. 18). The element mapping confirms the homogeneous distribution of C and O within the particles (Supplementary Fig. 18). X-ray photoelectron spectroscopy (XPS) further vindicates the crystal purity and shows atomic percentages of 29.9% Li and 45.1% O, with less than 0.1% Na (Fig. 4d). High-resolution XPS spectra of C 1s and O 1s confirm the presence of C=O and C-O bonds in those generated crystals (Supplementary Fig. 19). X-ray diffraction (XRD) analysis further confirms that all the crystals are  $\text{Li}_2\text{CO}_3$ , demonstrating a high product purity (Fig. 4e).

The temporal evolution of  $\text{Li}^+$  and  $\text{Na}^+$  concentrations in the bipolar membrane in-situ crystallization configuration is shown in Fig. 4f. At an optimized current density of  $5 \text{ mA cm}^{-2}$ , both  $\text{Li}^+$  and  $\text{Na}^+$  in the feed chamber decrease to an extremely low value. In the recovery chamber, the  $\text{Li}^+$  initially increases and then decreases to  $0.1 \text{ g L}^{-1}$  due to the in-situ crystallization of  $\text{Li}_2\text{CO}_3$  (reaction mechanisms are detailed in Supplementary Fig. 17). This process yields  $\text{Li}_2\text{CO}_3$  crystals with > 99.9% purity (Fig. 4g). Without in-situ crystallization, > 99.0% of both  $\text{Li}^+$  and  $\text{Na}^+$  would be recovered (Fig. 4g and Supplementary Fig. 20). With this optimized configuration, > 98.0% of  $\text{Li}^+$  is recovered from the leaching solution (achieves a recovery of 95.5% for  $\text{Li}^+$  in the whole process), and produces  $\text{Li}_2\text{CO}_3$  with > 99.9% purity. Additionally, the NaOH (> 97.5% recovery, > 95% purity) is recovered and reused as a basic solution in subsequent membrane metal-complexing ex-situ crystallization as well as membrane metal-extracting temporal crystallization configurations (Supplementary Fig. 21). High-purity HCl is generated for spent LIB dissolution and subsequent systems for divalent cation recovery.

This bipolar membrane in-situ crystallization system not only generates high-purity  $\text{Li}_2\text{CO}_3$  but also provides significant energy, economic and environmental benefits. The recovered  $\text{Li}_2\text{CO}_3$ , NaOH, and HCl mitigate environmental pollution of discharged metal ions and safety risks

associated with high metal ion concentrations while offering valuable ion resources for industrial applications. Measuring by economic efficiency of per \$ kg<sup>-1</sup> Li<sub>2</sub>CO<sub>3</sub>, as shown in Fig. 4h, the economic analysis reveals that the primary costs are energy consumption (1.10 \$ kg<sup>-1</sup> Li<sub>2</sub>CO<sub>3</sub>) and investment (membranes: 1.68 \$ kg<sup>-1</sup> Li<sub>2</sub>CO<sub>3</sub>, maintenance: 0.43 \$ kg<sup>-1</sup> Li<sub>2</sub>CO<sub>3</sub>). Given the current market price of Li<sub>2</sub>CO<sub>3</sub> (24.00 \$ kg<sup>-1</sup>), the system yields a profit of around 20.79 \$ kg<sup>-1</sup> Li<sub>2</sub>CO<sub>3</sub> (Supplementary Tables 10-11). Beyond the Li<sub>2</sub>CO<sub>3</sub> profits, this configuration also generates NaOH and HCl for supporting other LIB recycling configurations, along with environmental benefits such as CO<sub>2</sub> fixation and zero liquid discharge. Despite those advantages, the system faces limitations of the current electro-driven membranes due to the low ion throughput and poor anti-scaling properties (Supplementary Fig. 22 and Fig. 23). Future work should focus on improving electro-membrane performance to enhance the metal ion throughput and mitigate electro-membrane issues that enable more efficient and sustainable LIB recycling.

### **Recovery of Mn<sup>2+</sup>, Ni<sup>2+</sup>, and Co<sup>2+</sup>**

The tandem leaching streams from the selective membrane dual-stage distillation system contain Mn<sup>2+</sup>, Ni<sup>2+</sup> and Co<sup>2+</sup>, which are extracted as valuable metals from the black mass obtained after precise dismantling and separation of spent LIBs. To recover those metal ions, the membrane metal-complexing ex-situ crystallization, as well as membrane metal-extracting temporal crystallization configurations, are developed, as illustrated in Fig. 5a. These systems exploit differential coordination behavior of Mn<sup>2+</sup>, Ni<sup>2+</sup>, and Co<sup>2+</sup> to ethylenediaminetetraacetic acid (EDTA) and the extractant Cyanex 272 to selectively recover Mn<sub>3</sub>O<sub>4</sub>, Ni(OH)<sub>2</sub>, and Co(OH)<sub>2</sub>, respectively (Fig. 5b). According to coordination capacity to the EDTA complexing agent, in the membrane metal-complexing ex-situ crystallization configuration, Ni<sup>2+</sup> and Co<sup>2+</sup> exhibits significantly higher coordination capacity with EDTA than Mn<sup>2+</sup>, thus forming [EDTA-Ni]<sup>2-</sup> ( $K_{Ni} = 2.5 \times 10^{18}$ ) and [EDTA-Co]<sup>2-</sup> ( $K_{Co} = 2.8 \times 10^{16}$ ) (Supplementary Figs. 24-25). In contrast, Mn<sup>2+</sup> exhibits a significantly lower coordination capacity with EDTA ( $K_{Mn} = 7.8 \times 10^{13}$ ). Consequently,

Mn<sup>2+</sup> migrates to the recovery chamber, where it chemically reacts with the extra-added OH<sup>-</sup> (supplied from the bipolar membrane in-situ crystallization system) to precipitate as Mn(OH)<sub>2</sub>, which then is oxidized to Mn<sub>3</sub>O<sub>4</sub> under ambient conditions (25 °C) (Fig. 5ci). Following, the complexing anions of [EDTA-Ni]<sup>2-</sup> and [EDTA-Co]<sup>2-</sup> are retained in the collecting chamber of the membrane metal-complexing ex-situ crystallization system. The influence of the EDTA: (Ni+Co) molar ratio, including 0.95, 1.0, 1.05, and 1.15, on metal ion separation is explored (Supplementary Fig. 26). The concentration of Ni<sup>2+</sup>, Co<sup>2+</sup> and Mn<sup>2+</sup> in the feed chamber presented a decreasing trend (Figs. S26a-c). The Ni<sup>2+</sup> and Co<sup>2+</sup> form Ni[EDTA]<sup>2+</sup>/Co[EDTA]<sup>2+</sup> complex anions, thus they migrate towards the anode into the chamber. On the contrary, the Mn<sup>2+</sup> migrated towards the cathode into the recovery chamber as the experiment progressed (Supplementary Fig. 26f). A small amount of Ni<sup>2+</sup> and Co<sup>2+</sup> is also recovered along with Ni<sup>2+</sup> when the molar ratio of EDTA to Ni+Co at 1, due to the incomplete complexation (Supplementary Figs. 26d-e). As the molar ratio of EDTA to Ni+Co increases to 1.05, no extra Ni<sup>2+</sup> and Co<sup>2+</sup> ions are observed in the recovery chamber, and Mn<sup>2+</sup> approaches the highest recovery. However, a further increase in the molar ratio to 1.15 significantly decreased the recovery efficiency of Mn<sup>2+</sup> due to the formation of Mn[EDTA]<sup>2+</sup>. Considering the higher recovery of Mn<sup>2+</sup>, the molar ratio of EDTA to Ni+Co is optimized at 1.05. With the extra-added H<sup>+</sup>, which is supplied from the bipolar membrane in-situ crystallization, [EDTA-Ni]<sup>2-</sup> and [EDTA-Co]<sup>2-</sup> de-coordinate with EDTA, and the subsequent separation is carried out in the membrane metal-extracting temporal crystallization configuration. Based on the higher affinity capacity to Cyanex 272, the Co<sup>2+</sup> is more likely to form complex Co(Cyanex272)<sub>2</sub> and remain in the solution (Supplementary Figs. 27-28). Meanwhile, the Ni<sup>2+</sup> migrates to the recovery chamber under the electrical field and is finally recovered as the green crystal of Ni(OH)<sub>2</sub> (Fig. 5cii). With temporal control, the pink Co(OH)<sub>2</sub> is finally obtained from the extracted chamber of the membrane metal-extracting temporal crystallization system (Fig. 5ciii).

SEM imaging reveals distinct crystal morphologies with uniform elemental distribution for Mn, Ni and Co, respectively (Fig. 5d). Various specific crystal structures with different diameters and high homogeneity of the elements' distribution can be observed from those images. The XPS spectra results confirm high purity (> 99.5%) of all obtained metal ion products (Fig. 5e), with high-resolution spectra validating bonding environments of Mn, Ni and Co, respectively (Supplementary Figs. 29-31). The XRD analysis confirms phase-purity of the  $\text{Mn}_2\text{O}_3$ ,  $\text{Ni}(\text{OH})_2$  and  $\text{Co}(\text{OH})_2$ , respectively, with no other impurity peaks in each of the XRD spectra (Fig. 5f). The temporal evolution of  $\text{Ni}^{2+}$ ,  $\text{Co}^{2+}$  and  $\text{Mn}^{2+}$  concentrations in each chamber is measured using inductively coupled plasma optical emission spectrometry (ICP-OES). In the membrane metal-complexing ex-situ crystallization configuration (Fig. 5g), the  $\text{Ni}^{2+}$  and  $\text{Co}^{2+}$  form  $[\text{EDTA-Ni}]^{2-}$  and  $[\text{EDTA-Co}]^{2-}$  and migrate to the Ni & Co collect chamber in the anode side, while  $\text{Mn}^{2+}$ , which remains uncomplexed, transports towards the cathode into the Mn recovery chamber. Then  $[\text{EDTA-Ni}]^{2-}$  and  $[\text{EDTA-Co}]^{2-}$  are decomplexed using 2.0 M  $\text{H}_2\text{SO}_4$ , the collected Ni and Co solution is used in the next membrane metal-extracting temporal crystallization configuration (Fig. 5h). In the first 10 h, the  $\text{Co}^{2+}$  accumulates in the co-extraction chamber as the  $\text{Co}^{2+}$  complexes with Cyanex272, forming non-charged  $\text{Co}(\text{Cyanex272})_2$ , while positively charged  $\text{Ni}^{2+}$  migrates to the recovery chamber. After 10 h,  $\text{Co}(\text{Cyanex272})_2$  is dissociated into  $\text{Co}^{2+}$ , which is transported to the recovery chamber later.

In the membrane metal-complexing ex-situ crystallization system, with the optimized current density of  $5 \text{ mA cm}^{-2}$ , the results reveal more than 99.5%  $\text{Mn}^{2+}$  recovery, and yield  $\text{Mn}_3\text{O}_4$  with purity higher than 99.9% (Fig. 5i). Residual  $[\text{EDTA-Ni}]^{2-}$  and  $[\text{EDTA-Co}]^{2-}$  are retained in the collection chamber, ensuring freshwater reclamation and zero waste discharge. In the membrane metal-extracting temporal crystallization configuration, with optimized operating conditions,  $\text{Ni}^{2+}$  and  $\text{Co}^{2+}$  are recovered with recoveries of higher than 83.1% and 87.3%, generating the final products of  $\text{Ni}(\text{OH})_2$  and  $\text{Co}(\text{OH})_2$  with more than 99.5% and 92.5% purity, respectively (Fig. 5i).

The recovery of high-purity  $\text{Mn}_3\text{O}_4$ ,  $\text{Ni}(\text{OH})_2$ , and  $\text{Co}(\text{OH})_2$  not only addresses the heavy metal ion pollution but also delivers significant economic benefits. Taking  $\text{Mn}_3\text{O}_4$  as an example, in the membrane metal-complexing ex-situ crystallization configuration, taking the economic efficiency of per \$  $\text{kg}^{-1}$   $\text{Mn}_3\text{O}_4$ , the energy consumption and investment costs are 1.30 and 1.02 \$  $\text{kg}^{-1}$   $\text{Mn}_3\text{O}_4$ , respectively (Fig. 5j). With a market price of ~ 9.00 \$  $\text{kg}^{-1}$   $\text{Mn}_3\text{O}_4$ , this configuration yields profits of 6.68 \$  $\text{kg}^{-1}$   $\text{Mn}_3\text{O}_4$  (Supplementary Table 12). In the membrane metal-extracting temporal crystallization configuration, measured by economic efficiency of per \$  $\text{kg}^{-1}$  [ $\text{Ni}(\text{OH})_2 + \text{Co}(\text{OH})_2$ ] (with the mole ratio of 47:53), the energy consumption and investment costs are 1.89 and 1.86 \$  $\text{kg}^{-1}$  [ $\text{Ni}(\text{OH})_2 + \text{Co}(\text{OH})_2$ ], respectively (Fig. 5j). Given market prices of > 14 \$  $\text{kg}^{-1}$  for  $\text{Ni}(\text{OH})_2$  and > 18 \$  $\text{kg}^{-1}$  for  $\text{Co}(\text{OH})_2$ , this system brings a profit at least 12.37 \$  $\text{kg}^{-1}$  [ $\text{Ni}(\text{OH})_2 + \text{Co}(\text{OH})_2$ ] (Supplementary Table 13). Compared to the mainstream technologies for Li recovery, the e-MCGR technology not only achieves a lower overall cost but also offers distinct profit advantages (Supplementary Table 14). Besides these energy consumptions, the extra added NaOH and HCl are supplied and reused from the bipolar membrane in-situ crystallization system. The EDTA and the Cyanex 272 are recycled in membrane metal-complexing ex-situ crystallization and membrane metal-extracting temporal crystallization systems, which minimize reagent consumption and enhance the system's circularity. Considering the recovery rate of those metal ions, the profits could be improved when using the electro-driven membrane with high metal ion transport capacity in this configuration. Despite its energy, economic and environmental advantages, those systems face challenges, particularly mineral scaling on electro-membranes, which limits metal ion throughput and recovery efficiency (Supplementary Fig. 32). To address these limitations, future efforts should focus on designing electro-membranes with higher ion transport capacity and enhanced anti-scaling properties. A fundamental study in advancing the understanding of metal ion crystallization kinetics in electro-membrane systems is essential to optimize recovery processes.

## Recovery of metal ions from real LIBs leachate

The e-MCGR process for efficient LIBs recycling is further validated using real leachate from spent NMC111 cathode material (Fig. 6a). In the first-stage selective electro dialysis, operated at a current density of  $1.0 \text{ mA cm}^{-2}$ , the CIMS membranes effectively reject multivalent metal ions ( $\text{Mn}^{2+}$ ,  $\text{Ni}^{2+}$ , and  $\text{Co}^{2+}$ ) and permeate monovalent metal ions ( $\text{Na}^+$  and  $\text{Li}^+$ ). Thus, the concentrations of  $\text{Li}^+$  and  $\text{Na}^+$  increase to  $1.08 \text{ g L}^{-1}$  and  $3.73 \text{ g L}^{-1}$  in the recovery chamber, respectively (Fig. 6b). The residual solutions from the transitional chambers (in both transitional chamber-1 and transitional chamber-2) in the first-stage selective electro dialysis are then fed into the second-stage selective electro dialysis for further separation (Fig. 6c). This selective membrane dual-stage distillation configuration achieves accumulative recovery of 93.9% for  $\text{Li}^+$  and 89.1% for  $\text{Na}^+$ , while completely rejecting  $\text{Mn}^{2+}$ ,  $\text{Ni}^{2+}$  and  $\text{Co}^{2+}$ . This process demonstrated the low energy cost ( $1.56 \text{ \$ kg}^{-1}$ ), investment cost ( $7.08 \text{ \$ kg}^{-1}$ ), and energy consumption ( $14.87 \text{ kWh kg}^{-1}$ ) (Supplementary Table 15).

Subsequent bipolar membrane in-situ crystallization process recovers 96.6%  $\text{Li}^+$  from the leaching solution and produces  $\text{Li}_2\text{CO}_3$  with  $> 99.9\%$  purity (Figs. 6d-e). XPS analysis confirm the product's composition, showing atomic percentages of 32.2% Li, and 39.6% O, with others less than 0.3% (Fig. 6f). The high-purity of 99.9% was further verified by XRD analysis (Fig. 6g). The economic analysis reveals that the primary costs are energy consumption ( $0.72 \text{ \$ kg}^{-1} \text{ Li}_2\text{CO}_3$ ) and investment cost ( $2.12 \text{ \$ kg}^{-1} \text{ Li}_2\text{CO}_3$ ). Given the current market price of  $\text{Li}_2\text{CO}_3$  ( $24.00 \text{ \$ kg}^{-1}$ ), the system yields a profit of around  $21.16 \text{ \$ kg}^{-1} \text{ Li}_2\text{CO}_3$  (Supplementary Table 16). Moreover, 97.7% NaOH with 96.7% purity is recovered from the bipolar membrane in-situ crystallization process.

In membrane metal-complexing ex-situ crystallization, due to its lower coordination capacity with EDTA,  $\text{Mn}^{2+}$  migrates to the recovery chamber (Fig. 6h). In a separate membrane metal-extracting temporal crystallization step,  $\text{Ni}^{2+}$  migrates to the recovery chamber and is recovered as  $\text{Ni}(\text{OH})_2$  by adding NaOH (Fig. 6i). With temporal control, the pink  $\text{Co}(\text{OH})_2$  is subsequently

obtained from the extraction chamber. The membrane metal-complexing ex-situ crystallization proves optimal for maximizing the recovery rate and product purity for all transition metals (Fig. 6j). The XPS spectra results confirm high purity (> 92.0%) of all obtained metal ion products (Fig. 6k). The XRD analysis confirms the generation of  $\text{Mn}_3\text{O}_4$  (Fig. 6l). The energy consumption and investment costs are 1.42 and 1.46 \$  $\text{kg}^{-1}$   $\text{Mn}_3\text{O}_4$ , respectively. With a market price of ~ 9.00 \$  $\text{kg}^{-1}$   $\text{Mn}_3\text{O}_4$ , this configuration yields profits of 6.12 \$  $\text{kg}^{-1}$   $\text{Mn}_3\text{O}_4$  (Supplementary Table 17). XRD analysis confirmed the phase purity of the recovered  $\text{Ni}(\text{OH})_2$  and  $\text{Co}(\text{OH})_2$  (Figs. 6m-n). The process achieved an 80.1% recovery of  $\text{Ni}(\text{OH})_2$  with 99.3% purity and, with temporal control, a 95.6% recovery of pink  $\text{Co}(\text{OH})_2$  with 92.2% purity. The combined energy consumption and investment costs for recovering  $\text{Ni}(\text{OH})_2 + \text{Co}(\text{OH})_2$  are 1.61 and 1.93 \$  $\text{kg}^{-1}$  [ $\text{Ni}(\text{OH})_2 + \text{Co}(\text{OH})_2$ ], respectively. Given market prices of > 14 \$  $\text{kg}^{-1}$  for  $\text{Ni}(\text{OH})_2$  and > 18 \$  $\text{kg}^{-1}$  for  $\text{Co}(\text{OH})_2$ , this system brings a profit of 12.58 \$  $\text{kg}^{-1}$  [ $\text{Ni}(\text{OH})_2 + \text{Co}(\text{OH})_2$ ] (Supplementary Table 18).

## Discussion

This work presents a highly modular platform for recycling spent lithium-ion batteries (LIBs) through an electro-membrane crystallization-assisted general recycling (e-MCGR) concept and technology. This e-MCGR incorporates four key configurations: (1) selective membrane dual-stage distillation for  $\text{Li}^+$  and  $\text{Na}^+$  separation from multivalent cations ( $\text{Mn}^{2+}$ ,  $\text{Ni}^{2+}$ , and  $\text{Co}^{2+}$ ), (2) bipolar membrane in-situ crystallization for  $\text{Li}_2\text{CO}_3$  recovery and  $\text{CO}_2$  utilization, (3) membrane metal-complexing ex-situ crystallization for  $\text{Mn}_3\text{O}_4$  recovery, and (4) membrane metal-extracting temporal crystallization for  $\text{Ni}(\text{OH})_2$  and  $\text{Co}(\text{OH})_2$  recovery. These configurations enable the efficient separation and recovery of valuable metal ions, including  $\text{Li}^+$ ,  $\text{Mn}^{2+}$ ,  $\text{Ni}^{2+}$  and  $\text{Co}^{2+}$  from LIB leaching solutions, achieving high recoveries and crystal product purity. The proposed system not only addresses resource scarcity and environmental pollution but also delivers significant economic benefits. The recovery of high-purity  $\text{Li}_2\text{CO}_3$ ,  $\text{Mn}_3\text{O}_4$ ,  $\text{Ni}(\text{OH})_2$ , and  $\text{Co}(\text{OH})_2$  generates substantial profits, and the reuse of NaOH, HCl, and recycling of EDTA/Cyanex 272 minimize

waste and enhance sustainability. The novel design concepts, technological principles, and evaluation methods demonstrated in this work pave the way for the development of high-efficiency and economically viable LIB recycling systems. This e-MCGR technology can be integrated with intermittent energy systems and sustainable resource management. To further advance this technology, future efforts should focus on developing advanced electro-driven membranes with high metal ion permeation rates, enhanced target ion selectivity, and superior anti-scaling properties.

## Methods

### Pretreatment

The suspended solids in the feed are removed by using ultrafiltration (UP150 membrane) at an operating pressure of 0.01 MPa. Then the permeate is concentrated using reverse osmosis (RO, BW30 membrane) at an operating pressure of 1.5 MPa.

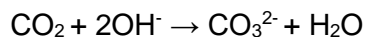
### Configurations in the e-MCGR process

All experimental configurations described herein were conducted using a single, consistently prepared complex feed batch (the composition is shown in Supplementary Table 7) to ensure comparability and integration across the e-MCGR process. This batch simulated real LIB leachate and was used sequentially across all experimental stages without intermediate reconstitution (Supplementary Table 19). The integrated design of the e-MCGR process comprises:

i. Selective membrane dual-stage distillation configuration: This configuration employs two sequential selective electro-membrane stacks to separate monovalent metal ions ( $\text{Li}^+$  and  $\text{Na}^+$ ) from the divalent metal ions ( $\text{Mn}^{2+}$ ,  $\text{Ni}^{2+}$  and  $\text{Co}^{2+}$ ). In the first-stage selective electro-membrane stack (Supplementary Fig. 6), the membranes are arranged as: anode / bipolar membrane (BM) / AMX (commercial anion exchange membrane)  $\times$  3 / CIMS (commercially monovalent cation exchange membrane)  $\times$  3 / bipolar membrane (BM) / cathode (Supplementary Table 20). The effective area per membrane is 0.0189 m<sup>2</sup>. Four chambers (feed, transitional-1, transitional-2, recovery) are connected to containers holding 2 L simulated LIB leaching solution in the feed

chamber and 0.5 L deionized water in the other chambers. The operational parameters of the current densities are tested at  $1 \text{ mA cm}^{-2}$ ,  $2.5 \text{ mA cm}^{-2}$ , and  $5 \text{ mA cm}^{-2}$ . The electric current of the electro-membrane stack is supplied by a stabilized power supply. In order to further distill  $\text{Li}^+$  and  $\text{Na}^+$  from transitional chambers (transitional chamber-1 and transitional chamber-2) of the first stage, the second-stage selective electro-membrane stack is developed (Supplementary Fig. 6), and the electro-membrane stack arrangement is anode / BM / AMX  $\times 2$  / CIMS  $\times 2$  / BM / cathode. Three chambers in the electro-membrane stack consist of the feed chamber, the transitional chamber, and the recovery chamber. For those chambers, 1 L of residual solution from the first-stage transitional chambers is introduced into the feed chamber of the second-stage stacks, and the transitional and recovery chambers are initially fed with 0.5 L of deionized water. The current density of the electro-membrane stack is  $0.5 \text{ mA cm}^{-2}$ . The refined  $\text{Li}^+$  and  $\text{Na}^+$  from the recovery chamber are then directly used as feed for the subsequent bipolar membrane in-situ crystallization (ii) to separate  $\text{Li}^+$  from  $\text{Na}^+$ .

ii. Bipolar membrane in-situ crystallization configuration: In this configuration, the electro-membranes are stacked between anode and cathode in a sequence of the anode / BM / AMX / commercial cation exchange membrane (CMX) / BM / cathode (Supplementary Fig. 13), forming three chambers, including the feed chamber, the acid chamber, and the base chamber. Specifically, 1 L monovalent metal ions solution ( $\text{Li}^+$  and  $\text{Na}^+$ ) from the recovery chambers of configuration (i) is used as the initial feed, and 0.5 L of deionized water is fed to the acid and base chambers. The electric current of this electro-membrane stack is  $5 \text{ mA cm}^{-2}$ , which is supplied by a direct current-stabilized power supply. To avoid  $\text{Na}^+$  impurities in  $\text{Li}_2\text{CO}_3$  (caused by  $\text{Na}_2\text{CO}_3$  co-precipitation) and capture the  $\text{CO}_2$  from industry,  $\text{CO}_2$  gas is introduced into the base chamber as a carbonate source, at a constant flow rate of  $50 \text{ mL min}^{-1}$  (Supplementary Fig. 14). During the reaction,  $\text{CO}_2$  dissolves into the solution and subsequently forms carbonate species. The  $\text{Li}_2\text{CO}_3$  crystals will be crystallized in the base solution, followed by  $\text{Li}_2\text{CO}_3$  recovery with the UP150 membrane.



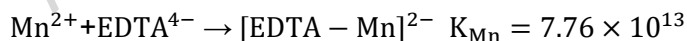
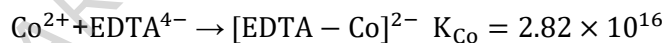
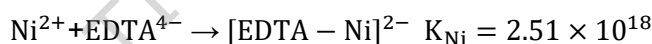
Then,  $\text{Li}_2\text{CO}_3$  crystallization occurs as



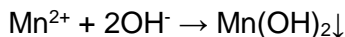
Overall, the reaction is



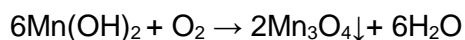
iii. Membrane metal-complexing ex-situ crystallization configuration: Here, the membrane sequence is: anode / CMX / AMX / CMX / AMX / cathode (Supplementary Fig. 19), with three chambers: the feed, complexing, and the recovery chamber. The residual divalent metal-rich solution remaining after configuration (i) serves as the feed for this configuration. Herein, 3.0 L mixtures of  $\text{Mn}^{2+}$ ,  $\text{Ni}^{2+}$ , and  $\text{Co}^{2+}$  are introduced into the feed chamber, and 0.5 L of deionized water is fed into the complexing and recovery chambers. The feed solution is further treated with the EDTA-4Na salt in the feed container. When the  $[\text{EDTA}]^{4-}$  forms complex anions with  $\text{Ni}^{2+}$  and  $\text{Co}^{2+}$ , with the EDTA's differential coordination capacities ( $K_{\text{Ni}} > K_{\text{Co}} \gg K_{\text{Mn}}$ ), the  $\text{Mn}^{2+}$  is separated from  $\text{Ni}^{2+}$  and  $\text{Co}^{2+}$  using this membrane metal-complexing ex-situ crystallization system,



For the decomplexation, EDTA complexes are dissociated by adding 2.0 M HCl until pH < 0.5. To recover metal ions,  $\text{Mn}^{2+}$  in the recovery chamber is precipitated as  $\text{Mn}(\text{OH})_2$  by using 1.0 M NaOH. Both the acid and base used here are provided by configuration (ii).

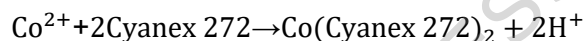


Then, the  $\text{Mn}(\text{OH})_2$  is oxidized to black  $\text{Mn}_3\text{O}_4$  crystals

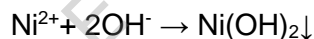


Membrane metal-extracting temporal crystallization configuration: Connecting with the membrane metal-complexing ex-situ crystallization configuration, this stack uses: anode / AMX / CMX / CMX

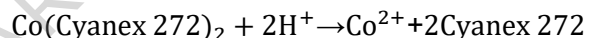
/ AMX / cathode (Supplementary Fig. 19). In this system, the membrane stack contains three containers, which connect with the feed chamber, the Co-extraction chamber, and the Ni-recovery chamber. The containers are initially fed with 0.5 L mixed Ni<sup>2+</sup> and Co<sup>2+</sup> solution from the membrane metal-complexing ex-situ crystallization system, 0.5 L extraction solution (50% saponified Cyanex 272 in kerosene), and 0.5 L deionized water, respectively. The electric current of the complexation electro dialysis stack is tested at 5 mA cm<sup>-2</sup>. Due to the Cyanex 272 preferentially binds Co<sup>2+</sup>, it enables efficient Ni<sup>2+</sup> and Co<sup>2+</sup> separation. In this process, the Co<sup>2+</sup> is extracted by Cyanex 272, which forms a stable complex with Cyanex 272 in the extraction chamber.



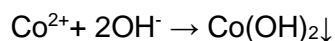
Then, the uncomplexed Ni<sup>2+</sup> migrates to the Ni-recovery chamber under the electric field. The Ni<sup>2+</sup> is precipitated as Ni(OH)<sub>2</sub> with the usage of 1.0 M NaOH (supplied from the bipolar membrane in-situ crystallization system).



With temporal crystallization of Ni<sup>2+</sup>, 2.0 M HCl is added to the feed chamber to release CO<sup>2+</sup> from Cyanex 272,



Then, these Co<sup>2+</sup> migrate to the Co-recovery chamber under the electric field and precipitate as Co(OH)<sub>2</sub> with the usage of 1.0 M NaOH.



### Validation of the e-MCGR process using real LIBs wastewater

To validate the practical feasibility of the e-MCGR process, real wastewater from spent ternary LIBs is used as feed. The spent ternary LIBs, sourced from a technology company's power bank, are used as the primary raw materials. First, 0.4 g of waste NMC111 cathode material is leached in 4.0 M HCl at 80 °C for 6 h. The resulting leachate is subjected to the same pretreatment sequence as described in Section "Pretreatment," namely ultrafiltration (UP150 membrane, 0.01

MPa) to remove organic impurities, followed by RO (BW30 membrane, 1.5 MPa) to concentrate the solution. The concentrated leachate, now enriched in  $\text{Li}^+$ ,  $\text{Na}^+$ ,  $\text{Mn}^{2+}$ ,  $\text{Ni}^{2+}$ , and  $\text{Co}^{2+}$ , is directly used as the feed for the e-MCGR process, without reconstitution or modification, to ensure a one-to-one comparison with the results obtained from the simulated LIB leachate.

### Characterization methods

The chemical composition and bonding states of the recovered crystals are analyzed by using X-ray photoelectron spectroscopy (XPS; AXIS UltraDLD, Shimadzu, Japan). Scanning electron microscopy (SEM; Sirion 200, FEI, USA) coupled with energy-dispersive spectroscopy (EDS; INCA X-Act, USA) is employed to assess crystal morphology, surface roughness, and elemental distribution. The crystal phase identification is performed through X-ray diffractometry (XRD; XRD-6100, Shimadzu, Japan) using  $\text{Cu-K}\alpha$  radiation ( $\lambda = 1.5 \text{ \AA}$ ). Metal ion concentrations are quantified by using Inductively Coupled Plasma Optical Emission spectroscopy (ICP-OES; Avio 500, PerkinElmer, USA). The properties of ion exchange membranes used in the study are shown in Supplementary Table 12.

### Evaluation methods

Technological analysis

Metal ion selectivity ( $P$ ) is a parameter that is used to illustrate membrane selectivity compared to other ions. Compared to other metal ions ( $M^{z+}$ ), the target metal ion selectivity can be calculated as

$$P = \frac{T_{\text{target}}/T_m}{c_{\text{target}}/c_m} = \frac{J_{\text{target}} \cdot c_m}{J_m \cdot c_{\text{target}}} \quad (1)$$

Where  $T_{\text{target}}$  and  $T_m$  are the transport numbers of target metal ions and other metal ions.  $c$  ( $\text{mol L}^{-1}$ ) is the concentration of metal ions.  $J$  ( $\text{eq./m}^2 \cdot \text{s}$ ) is the metal ion permeation rate, which is used to illustrate ion transport capacity, and can be calculated as

$$J = \frac{V \cdot \frac{dc}{dt}}{S} \quad (2)$$

Where  $V$  (mL) is the volume of solution, and  $S$  (cm<sup>2</sup>) is the membrane area.

The product recovery rate ( $R$ , %) is calculated by,

$$R = \frac{m_t}{m} \quad (3)$$

where  $m_t$  (g) is the mass of precipitate recovered at time  $t$ , and  $m$  (g) is the theoretical maximum precipitate mass.

The equation of total suspended solids measurement, which is the crystal yield ( $Y$ , g L<sup>-1</sup>),

$$Y = \frac{m_{cry}}{V_{brine}} \quad (4)$$

where  $m_{cry}$  is the mass of dried crystals, and  $V_{brine}$  (L) is the volume of feed wastewater.

Energy, economic and environmental analysis

In this e-MCGR process, the specific energy consumption ( $E$ , kWh kg<sup>-1</sup>) is calculated by,

$$E = \int_0^t \frac{U_t I dt}{C_t V_t M} \quad (5)$$

where  $U_t$  (V) is the electro-membrane stack voltage,  $I$  (A) is the current,  $V_t$  (L) is the volume of solution,  $C_t$  (mol L<sup>-1</sup>) is the concentration, and  $M$  (g mol<sup>-1</sup>) is the molecular mass. More data on energy, economics and the environment on this e-MCGR technology are analyzed and summarized in the Supplementary Information.

### Data availability

The data generated in this study are provided in the article and its Supplementary Information. Visualization and figure preparation are carried out using Origin 8, Microsoft PowerPoint 2021, and Microsoft Excel 2021. Source data are provided with this paper.

### References

- 1 Pomerantseva, E. et al. Energy storage: The future enabled by nanomaterials. *Science* **366**, eaan8285 (2019).

- 2 Tao, Y. et al. Second life and recycling: Energy and environmental sustainability perspectives for high-performance lithium-ion batteries. *Sci. Adv.* **7**, eabi7633 (2021).
- 3 Harper, G. et al. Recycling lithium-ion batteries from electric vehicles. *Nature* **575**, 75-86 (2019).
- 4 Niu, B. et al. Recycling hazardous and valuable electrolyte in spent lithium-ion batteries: urgency, progress, challenge, and viable approach. *Chem. Rev.* **123**, 8718-8735 (2023).
- 5 Ma, R. et al. Pathway decisions for reuse and recycling of retired lithium-ion batteries considering economic and environmental functions. *Nat. Commun.* **15**, 7641 (2024).
- 6 Ji, G. et al. Direct regeneration of degraded lithium-ion battery cathodes with a multifunctional organic lithium salt. *Nat. Commun.* **14**, 584 (2023).
- 7 Baars, J. et al. Circular economy strategies for electric vehicle batteries reduce reliance on raw materials. *Nat. Sustain.* **4**, 71-79 (2020).
- 8 Yang, T. et al. Sustainable regeneration of spent cathodes for lithium-ion and post-lithium-ion batteries. *Nature Sustain.* **7**, 776-785 (2024).
- 9 Kim, K. et al. Selective cobalt and nickel electrodeposition for lithium-ion battery recycling through integrated electrolyte and interface control. *Nat. Commun.* **12**, 6554 (2021).
- 10 Zhao, Y. et al. Recycling of sodium-ion batteries. *Nat. Rev. Mater.* **8**, 623-634 (2023).
- 11 Kazi, O. A. et al. Material design strategies for recovery of critical resources from water. *Adv. Mater.* **35**, e2300913 (2023).
- 12 Ji, G. et al. Sustainable upcycling of mixed spent cathodes to a high-voltage polyanionic cathode material. *Nat. Commun.* **15**, 4086 (2024).
- 13 Zhao, Y. et al. Advanced ion transfer materials in electro-driven membrane processes for sustainable ion-resource extraction and recovery. *Prog. Mater. Sci.* **128**, 100958 (2022).
- 14 Xu, X. et al. Extraction of lithium with functionalized lithium ion-sieves. *Prog. Mater. Sci.* **84**, 276-313 (2016).

- 15 Srimuk, P. et al. Charge-transfer materials for electrochemical water desalination, ion separation and the recovery of elements. *Nat. Rev. Mater.* **5**, 517-538 (2020).
- 16 Lei, S., Sun, W. & Yang, Y. Solvent extraction for recycling of spent lithium-ion batteries. *J. Hazard. Mater.* **424**, 127654 (2022).
- 17 Krishnan, S. et al. Current technologies for recovery of metals from industrial wastes: An overview. *Environ. Technol. Inno.* **22**, 101525 (2021).
- 18 Mossali, E. et al. Lithium-ion batteries towards circular economy: A literature review of opportunities and issues of recycling treatments. *J. Environ. Manage.* **264**, 110500 (2020).
- 19 Wang, M. et al. Selective Extraction of Critical Metals from Spent Lithium-Ion Batteries. *Environ. Sci. Technol.* **57**, 3940-3950 (2023).
- 20 Uliana, A. A. et al. Ion-capture electro dialysis using multifunctional adsorptive membranes. *Science* **372**, 296-299 (2021).
- 21 Tan, R. et al. Hydrophilic microporous membranes for selective ion separation and flow-battery energy storage. *Nat. Mater.* **19**, 195-202 (2020).
- 22 Liu, Y. et al. Pillared Lamellar vermiculite membranes with tunable monovalent and multivalent ion selectivity. *Adv. Mater.* e2417994 (2025).
- 23 Zhao, Y. et al. Self-assembled embedding of ion exchange materials into nanofiber-based hydrogel framework for fluoride capture. *Chem. Eng. J.* **431**, 134201 (2022).
- 24 Qiu, Y. et al. Recovery of fluoride-rich and silica-rich wastewaters as valuable resources: a resource capture ultrafiltration-bipolar membrane electro dialysis-based closed-loop process. *Environ. Sci. Technol.* **56**, 16221-16229 (2022).
- 25 Chang, X. et al. Selective extraction of transition metals from spent  $\text{Li}_{1-x}\text{Co}_y\text{Mn}_{1-x-y}\text{O}_2$  cathode via regulation of coordination environment. *Angew. Chem. Int. Edit.* **61**, e202202558 (2022).

- 26 Ma, H. et al. Dual-channel-ion conductor membrane for low-energy lithium extraction. *Environ. Sci. Technol.* **57**, 17246-17255 (2023).
- 27 Wang, B. et al. Efficient separation and recovery of cobalt(II) and lithium(I) from spent lithium ion batteries (LIBs) by polymer inclusion membrane electrodialysis (PIMED). *Chem. Eng. J.* **430**, 132924 (2022).
- 28 Zhao, Y. et al. Formation of morphologically confined nanospaces via self-assembly of graphene and nanospheres for selective separation of lithium. *J. Mater. Chem. A* **6**, 18859-18864 (2018).
- 29 Zhao, Y. et al. Electric field-based ionic control of selective separation layers. *J. Mater. Chem. A* **8**, 4244-4251 (2020).
- 30 Yang, D. et al. Solution-processable polymer membranes with hydrophilic subnanometre pores for sustainable lithium extraction. *Nat. Water* (2025).
- 31 Zuo, P. et al. Near-frictionless ion transport within triazine framework membranes. *Nature* **617**, 299-305 (2023).
- 32 Lu, J. et al. Efficient metal ion sieving in rectifying subnanochannels enabled by metal-organic frameworks. *Nat. Mater.* **19**, 767-774 (2020).
- 33 Xu, J. et al. A green and sustainable strategy toward lithium resources recycling from spent batteries. *Sci. Adv.* **8**, eabq7948 (2022).
- 34 Qiu, Y. et al. Investigation of fluoride and silica removal from semiconductor wastewaters with a clean coagulation-ultrafiltration process. *Chem. Eng. J.* **438**, 135562 (2022).
- 35 Ciez, R. E. & Whitacre, J. F. Examining different recycling processes for lithium-ion batteries. *Nat. Sustain.* **2**, 148-156 (2019).
- 36 Wang, J. et al. Direct recycling of spent cathode material at ambient conditions via spontaneous lithiation. *Nat. Sustain.* **7**, 1283-1293 (2024).

- 37 Pan, J. et al. Preparation of a monovalent selective anion exchange membrane through constructing a covalently crosslinked interface by electro-deposition of polyethyleneimine. *J. Membrane Sci.* **539**, 263-272 (2017).
- 38 Qiu, Y. et al. Ionic resource recovery for carbon neutral papermaking wastewater reclamation by a chemical self-sufficiency zero liquid discharge system. *Water Res.* **229**, 119451 (2023).
- 39 Liu, Y., Zhu, Y. & Cui, Y. Challenges and opportunities towards fast-charging battery materials. *Nat. Energy* **4**, 540-550 (2019).
- 40 Liu, K. et al. Ion-Ion selectivity of synthetic membranes with confined nanostructures. *ACS Nano* **18**, 21633-21650 (2024).
- 41 Kang, Y. et al. Nanoconfinement enabled non-covalently decorated MXene membranes for ion-sieving. *Nat. Commun.* **14**, 4075 (2023).
- 42 Xu, T. et al. Highly ion-permselective porous organic cage membranes with hierarchical channels. *J. Am. Chem. Soc.* **144**, 10220-10229 (2022).
- 43 Xu, T. et al. Perfect confinement of crown ethers in MOF membrane for complete dehydration and fast transport of monovalent ions. *Sci. Adv.* **10**, eadn0944 (2024).
- 44 Zhang, H. et al. Ultrafast selective transport of alkali metal ions in metal organic frameworks with subnanometer pores. *Sci. Adv.* **4**, eaaq0066 (2018).
- 45 Lu, J. et al. An artificial sodium-selective subnanochannel. *Sci. Adv.* **9**, eabq1369 (2023).
- 46 Zhang, H. et al. Angstrom-scale ion channels towards single-ion selectivity. *Chem. Soc. Rev.* **51**, 2224-2254 (2022).
- 47 Li, H. et al. A contact-electro-catalytic cathode recycling method for spent lithium-ion batteries. *Nat. Energy* **8**, 1137-1144 (2023).
- 48 Jiang, C. et al. Ion-“distillation” for isolating lithium from lake brine. *AIChE J.* **68**, 17710 (2022).

49 Lu, G. et al. Nano-confined controllable crystallization in supramolecular polymeric membranes for ultra-selective desalination. *Nat. Commun.* **16**, 2284 (2025).

### Acknowledgements

This work was supported by the Innovation and Technology Support Program Seed Application (No. ITS/332/23, Y.Z.), the RGC General Research Fund (No. 17203924, Y.Z.), and the National Natural Science Foundation (No. 22308288, Y.Z.). Y.Z. and B.V.B. acknowledge the support provided by the Fonds Wetenschappelijk Onderzoek - Vlaanderen (FWO) (No. 12A6823N and V461824N). L.X. acknowledges the support from the Fonds Wetenschappelijk Onderzoek – Vlaanderen (FWO) (No. 12B1E24N). X.Z. and S.D. acknowledge the support from the NSF Great Lakes ReNEW Water Innovation Engine (No. 2315268).

### Author contributions

Y.Z. conceived and designed the experiments. Y.Z., Y.Q. and L.X. supervised the study and experiments. Y.Z., Y.Q. and L.X. conducted the membrane fabrication, characterization, and performance tests. C.Y.T. and B.V.B. provided resources for project implementation. Y.Z., Y.Q. and L.X. designed and performed the calculation. C.Y.T. and B.V.B. supported experimental results. Y.Z. wrote the paper. X.Z., S.Z., G.L., J.S., R.D. and S. D assisted in results discussion. All the authors provided comments and revised the manuscript.

### Competing interests

The authors declare no competing interests.

### Figure Legends

**Fig. 1 Global overview of lithium-ion battery development in 2024.** a, Global lithium-ion battery production breakdown by region in 2024 (GWh), a visual representation of regional contributions to global lithium-ion battery (LIB) manufacturing, measured in gigawatt-hours (GWh);

**b**, Global distribution of spent lithium-ion batteries in 2024 (Kt). The corresponding references are provided in Supplementary Tables 2 and 4.

**Fig. 2. Schematic of sustainable lithium-ion battery recycling process based on the concept of the e-MCGR with the design of multiple e-MC configurations by utilizing existing mature membranes.** (i) separation of monovalent cations ( $\text{Li}^+$  and  $\text{Na}^+$ ) from divalent cations ( $\text{Mn}^{2+}$ ,  $\text{Ni}^{2+}$  and  $\text{Co}^{2+}$ ) by using the selective membrane dual-stage distillation technology. UF: ultrafiltration. RO: reverse osmosis. SED: monovalent selective electrodialysis; (ii) separation of  $\text{Li}^+$  from  $\text{Na}^+$  via bipolar membrane in-situ crystallization technology, and enabling the recovery of high-purity  $\text{Li}_2\text{CO}_3$ . MC: membrane contactor. BMED-C: bipolar membrane crystallization; (iii) separation of divalent cations from each other (i.e.,  $\text{Mn}^{2+}$ ,  $\text{Ni}^{2+}$  and  $\text{Co}^{2+}$ ) through the membrane metal-complexing ex-situ crystallization (Complexing ED-C) as well as membrane metal-extracting temporal crystallization technology (Extracting ED-C), where  $\text{Mn}^{2+}$  is separated from  $\text{Ni}^{2+}$  and  $\text{Co}^{2+}$  via metal-complexing ex-situ crystallization configuration, yielding high-purity  $\text{Mn}_3\text{O}_4$ , followed by  $\text{Ni}^{2+}$  separation from  $\text{Co}^{2+}$  via membrane metal-extracting temporal crystallization configuration, producing high-purity  $\text{Ni}(\text{OH})_2$  and  $\text{Co}(\text{OH})_2$ , respectively. Details of the concept of e-MCGR are provided in Supplementary Fig. 4.

**Fig. 3. Selective separation of monovalent cations from concentrated LIB leaching solutions.** **a**, Schematic representation of the selective electrodialysis system and mechanisms governing metal ion selectivity, including size exclusion, electrostatic repulsion, and chemical affinity; **b**, Color evolution of the leaching solution during separation: from dark brown (initial solution) transitions to dark red ( $\text{Mn}^{2+}$ ,  $\text{Ni}^{2+}$  and  $\text{Co}^{2+}$  -rich solution) and colorless ( $\text{Li}^+$  and  $\text{Na}^+$  -rich solution); **c**, First-stage selective electrodialysis separation of 4 L leaching solution, showing changes in metal ion concentrations ( $\text{Li}^+$ ,  $\text{Na}^+$ ,  $\text{Mn}^{2+}$ ,  $\text{Ni}^{2+}$  and  $\text{Co}^{2+}$ ) across feed, transitional-1, transitional-2, and recovery chambers under the current density of  $1.0 \text{ mA cm}^{-2}$ ; **d**, Second-stage selective electrodialysis separation of 2 L transitional solution, tracking concentration changes in

feed, transitional and recovery chambers; **e**, Separation efficiency: the cumulative recovery rates of monovalent cations ( $\text{Li}^+$ : 96.5%,  $\text{Na}^+$ : 96.4%) and rejection rates of multivalent cations ( $\text{Mn}^{2+}$ ,  $\text{Ni}^{2+}$  and  $\text{Co}^{2+}$ : 100%); **f**, The energy, economic, and environmental analysis of energy consumption, energy cost, and investment cost for  $\text{Li}^+$  recovery; **g**, Optimized selective membrane dual-stage distillation performance metrics, including recovery rate (96.5%), purity (100%), and associated energy, economic and environmental costs under current density of first-stage at  $1 \text{ mA cm}^{-2}$  and second-stage at  $0.5 \text{ mA cm}^{-2}$ .  $R_m$ : monovalent metal ion recovery rate.  $P_{\text{Li}}$ : purity of recovered  $\text{Li}^+$ .  $C_i$ : investment cost.  $C_{\text{Li}}$ :  $\text{Li}^+$  recovery cost.  $C_e$ : energy cost. EC: energy consumption. Error bars denote the standard deviation of the means ( $n = 2$ ). Source data are provided as a Source data file.

**Fig. 4. Sustainable lithium carbonate ( $\text{Li}_2\text{CO}_3$ ) production from monovalent cation solution and waste  $\text{CO}_2$ .** **a**, Schematic of  $\text{Li}^+$  recovery via the bipolar membrane in-situ crystallization configuration and the mechanisms of  $\text{Li}_2\text{CO}_3$  formation through utilization; **b**, Operational principles of the bipolar membrane in-situ crystallization system, with an inset showing the collected  $\text{Li}_2\text{CO}_3$  powder (white); **c**, SEM images of the  $\text{Li}_2\text{CO}_3$  crystals (regular octahedral morphology,  $\sim 4 \mu\text{m}$  average diameter) and element mapping of C and O distribution; **d**, XPS survey spectra of the  $\text{Li}_2\text{CO}_3$  crystals, showing atomic percentages: Li (24.9%), O (45.1%), negligible Na ( $< 0.1\%$ ), and C (24.9%, with testing background); **e**, XRD spectra of the synthesized crystals, confirming the crystallographic phase of  $\text{Li}_2\text{CO}_3$ . All diffraction peaks align with the standard reference pattern for lithium carbonate (PDF#22-1141), demonstrating high phase purity and crystallinity.; **f**, Temporal evolution of  $\text{Li}^+$  and  $\text{Na}^+$  concentrations in feed and recovery chambers under optimized current density ( $5 \text{ mA cm}^{-2}$ ),  $\text{Li}^+$  depletion correlates with  $\text{Li}_2\text{CO}_3$  crystallization, error bars denote the standard deviation of the means ( $n = 2$ ); **g**, Recovery rates ( $\text{Li}^+$ : 98.0%;  $\text{Na}^+$ : 97.5%) and product purity ( $\text{Li}_2\text{CO}_3$ :  $> 99.9\%$ ;  $\text{NaOH}$ : 95%); **h**, The energy, economic and environmental analysis of the bipolar membrane in-situ crystallization system:

energy cost (1.10 \$ kg<sup>-1</sup> Li<sub>2</sub>CO<sub>3</sub>), investment (2.11 \$ kg<sup>-1</sup> Li<sub>2</sub>CO<sub>3</sub>), and profits (20.79 \$ kg<sup>-1</sup> Li<sub>2</sub>CO<sub>3</sub>) relative to market price of Li<sub>2</sub>CO<sub>3</sub> (24.00 \$ kg<sup>-1</sup>). Source data are provided as a Source data file.

**Fig. 5. Recycling of Mn<sup>2+</sup>, Ni<sup>2+</sup>, and Co<sup>2+</sup> from the divalent cation solutions.** **a**, Schematic of the subsequent membrane metal-complexing ex-situ crystallization as well as membrane metal-extracting temporal crystallization configurations for sequential separation of Mn<sup>2+</sup>, Ni<sup>2+</sup>, and Co<sup>2+</sup>; **b**, Mechanisms of the EDTA complexation (selective coordination with Ni<sup>2+</sup> and Co<sup>2+</sup>) and the Cyanex 272 extraction (preferential binding to Co<sup>2+</sup>), enabling targeted metal recovery; **c**, Photographs of recovered products, (i) black Mn<sub>3</sub>O<sub>4</sub>, (ii) green Ni(OH)<sub>2</sub>, and (iii) pink Co(OH)<sub>2</sub> powders; **d**, SEM images and elemental mapping of Mn<sub>3</sub>O<sub>4</sub>, Ni(OH)<sub>2</sub> and Co(OH)<sub>2</sub> crystals, respectively, confirming uniform morphology and homogeneous distribution of Mn, Ni, and Co; **e**, XPS spectra showing atomic compositions of (i) Mn<sub>3</sub>O<sub>4</sub> (Mn: 26.9%, O: 37.6%), (ii) Ni(OH)<sub>2</sub> (Ni: 29.1%, O: 56.3%), and (iii) Co(OH)<sub>2</sub> (Co: 23.7%, O: 54.9%), with < 0.1% impurities; **f**, XRD spectra confirming phase-pure Mn<sub>3</sub>O<sub>4</sub> (PDF#24-0734), Ni(OH)<sub>2</sub> (PDF#14-0117), and Co(OH)<sub>2</sub> (PDF#30-0443) powders, with no impurity peaks; **g**, Temporal evolution of Mn<sup>2+</sup>, Ni<sup>2+</sup>, and Co<sup>2+</sup> concentrations in membrane metal-complexing ex-situ crystallization system, achieving > 99.5% Mn<sup>2+</sup> at 5 mA cm<sup>-2</sup> and at EDTA : (Ni + Co) of 1.05; **h**, Temporal evolution of Ni<sup>2+</sup> and Co<sup>2+</sup> concentrations in membrane metal-extracting temporal crystallization system, recovering > 83.1% Ni<sup>2+</sup> and > 87.3% Co<sup>2+</sup>; **i**, Recovery and product purity of Mn<sub>3</sub>O<sub>4</sub> (> 99.5% recovery, > 99.9% purity), Ni(OH)<sub>2</sub> (> 83.1% recovery, > 99.5% purity), and Co(OH)<sub>2</sub> (> 87.3% recovery, > 92.5% purity). **j**, The energy, economic, and environmental analysis: energy consumption (Mn<sub>3</sub>O<sub>4</sub>: 1.30 \$ kg<sup>-1</sup> Mn<sub>3</sub>O<sub>4</sub>; Ni(OH)<sub>2</sub> and Co(OH)<sub>2</sub>: 1.89 \$ kg<sup>-1</sup> [Ni(OH)<sub>2</sub> + Co(OH)<sub>2</sub>]), investment costs (Mn<sub>3</sub>O<sub>4</sub>: 1.02 \$ kg<sup>-1</sup> Mn<sub>3</sub>O<sub>4</sub>; Ni(OH)<sub>2</sub> and Co(OH)<sub>2</sub>: 1.86 \$ kg<sup>-1</sup> [Ni(OH)<sub>2</sub> + Co(OH)<sub>2</sub>]), and net profits (Mn<sub>3</sub>O<sub>4</sub>: 6.68 \$ kg<sup>-1</sup> Mn<sub>3</sub>O<sub>4</sub>; Ni(OH)<sub>2</sub> and Co(OH)<sub>2</sub>: 12.37 \$ kg<sup>-1</sup> [Ni(OH)<sub>2</sub> + Co(OH)<sub>2</sub>]). Error bars denote the standard deviation of the means (n = 2). Source data are provided as a Source data file.

**Fig. 6. Recovery of lithium and metal salts from real LIBs leaching solutions.** **a**, Photo of spent LIBs leachate; **b**, First-stage selective electrodialysis separation of monovalent cations ( $\text{Li}^+$  and  $\text{Na}^+$ ) from divalent cations ( $\text{Mn}^{2+}$ ,  $\text{Ni}^{2+}$ , and  $\text{Co}^{2+}$ ) under the current density of  $1.0 \text{ mA cm}^{-2}$ ; **c**, Second-stage selective electrodialysis separation of transitional solution for enhanced monovalent selectivity; **d**, Temporal evolution of  $\text{Li}^+$  and  $\text{Na}^+$  concentrations under current density of  $5 \text{ mA cm}^{-2}$  in bipolar membrane in-situ crystallization process; **e**, Recovery rates and product purity; **f**, XPS spectra showing atomic compositions of  $\text{Li}_2\text{CO}_3$  crystals (Li : 30.2%, O: 44.8%, C: 24.8%); **g**, XRD spectra of the synthesized crystals; **h**, Temporal evolution of  $\text{Mn}^{2+}$ ,  $\text{Ni}^{2+}$ , and  $\text{Co}^{2+}$  concentrations in membrane metal-complexing ex-situ crystallization system; **i**, Temporal evolution of  $\text{Ni}^{2+}$  and  $\text{Co}^{2+}$  concentrations in membrane metal-extracting temporal crystallization system; **j**, Recovery and product purity of  $\text{Mn}_3\text{O}_4$  (> 94.5% recovery, >99.8% purity),  $\text{Ni}(\text{OH})_2$  (> 80.1% recovery, > 99.3% purity), and  $\text{Co}(\text{OH})_2$  (> 95.6% recovery, > 92.2% purity); **k**, XPS spectra showing atomic compositions of (i)  $\text{Mn}_3\text{O}_4$  (Mn: 27.4%, O: 31.3%), with < 0.3% impurities, (ii)  $\text{Ni}(\text{OH})_2$  (Ni: 29.6%, O: 46.3%), and (iii)  $\text{Co}(\text{OH})_2$  (Co: 24.8%, O: 42.4%), with < 1.0% impurities; **l**, XRD spectra confirming phase-pure  $\text{Mn}_3\text{O}_4$  (PDF#24-0734) powder; **m**, XRD spectra confirming phase-pure  $\text{Ni}(\text{OH})_2$  (PDF#14-0117) powder; **n**, XRD spectra confirming phase-pure  $\text{Co}(\text{OH})_2$  (PDF#30-0443) powder. Error bars denote the standard deviation of the means ( $n = 2$ ). Source data are provided as a Source data file.

### Editorial Summary

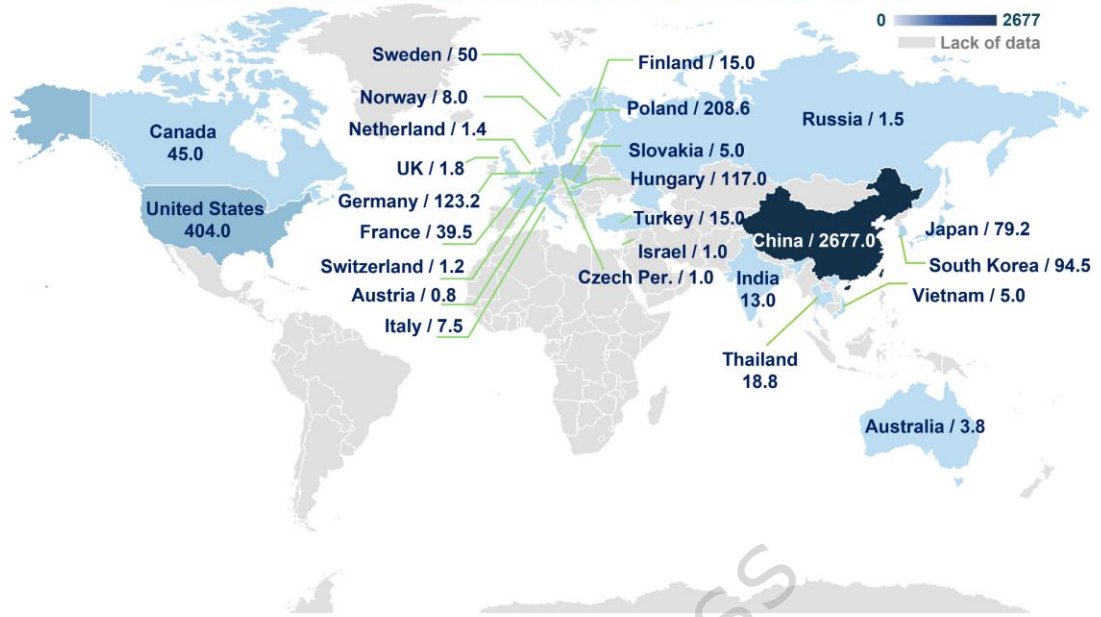
This study presents a scalable and sustainable electro-membrane crystallization-assisted general recycling technology that efficiently recovers high-purity lithium, manganese, nickel, and cobalt from spent lithium-ion batteries.

**Peer review information:** *Nature Communications* thanks the anonymous reviewers for their contribution to the peer review of this work. A peer review file is available.

ARTICLE IN PRESS

a.

Global lithium-ion battery production distribution in 2024 (GWh)



b.

Globally approximately spent lithium-ion battery distribution in 2024 (Kilotons)

